NANO · MICRO small
www.small-journal.com

Synergistic Optimization of Buried Interface via Hydrochloric Acid for Efficient and Stable Perovskite Solar Cells

*Xing Zhao, Danxia Wu, Huilin Yan, Peng Cui, Yujie Qiu, Bingbing Fan, Xiaopeng Yue, Liang Li, and Meicheng Li**

Incorporating chlorine into the SnO_2 electron transport layer (ETL) has proven effective in enhancing the interfacial contact between SnO_2 and perovskite in perovskite solar cells (PSCs). However, previous studies have primarily focused on the role of chlorine in passivating surface trap defects in SnO_2, without considering its influence on the buried interface. Here, hydrochloric acid (HCl) is introduced as a chlorine source into commercial SnO_2 to form Cl-capped SnO_2 (Cl-SnO_2) ETL, aiming to optimize the buried interface of the PSC. The incorporation of HCl into the SnO_2 precursor solution works in two key ways. First, it converts the detrimental KOH stabilizer into KCl through an acid-base reaction. Second, it regulates the crystallization process of the perovskite, reducing PbI_2 residues and voids at the buried interface. As a result, the efficiency of the PSC increases from 21.93% to 25.39%, with a certified efficiency of 25.69%, the highest efficiency reported for Cl-SnO_2 ETL-based PSCs. Moreover, the target PSC exhibits excellent air stability, retaining 90% of its initial efficiency after 2900 h of air exposure, compared to only 56.1% for the control PSC. This investigation highlights the effectiveness of HCl in the synergistic optimization of the buried interface in PSCs.

1. Introduction

Organic–inorganic hybrid perovskite solar cells (PSCs) have gained significant attention in both academia and industry due to their excellent advantages, such as a high absorption coefficient, long carrier diffusion length, easy fabrication process, and low cost.[1–3] These advantages have contributed to the remarkable increase in the power conversion efficiency (PCE) of PSCs, which has risen from 3.8% to a present certified efficiency of over 26%.[4,5] However, despite these advancements, PSCs still face serious challenges, particularly related to the buried interface, which has a high presence of trap defects and impurities.[6] These defects not only capture and hinder the movement of charge carriers but also can initiate chemical reactions that cause the decomposition of the perovskite material, deteriorating the efficiency and stability of PSCs.[7–9]

The quality of the buried interface in conventional n–i–p structured PSCs is directly influenced by the chemical properties of electron transport layers (ETLs).[10,11] The ETL prepared from commercial colloidal SnO_2 solution (Alfa Aesar) exhibited excellent chemical stability and reproducibility, demonstrating strong potential for large-scale industrial applications.[12] However, it has been reported that KOH is used as a stabilizer in the commercial SnO_2 solution to maintain suspension stability.[13,14] Although KOH can improve efficiency to some extent,[9] its strong alkalinity (pH≈11) and corrosiveness negatively impact the photovoltaic performance of PSCs.[15,16] On one hand, the surface of SnO_2 nanoparticles contains a high concentration of OH^- ions, which act as defects, trapping charge carriers at the buried interface.[17] On the other hand, KOH can interact with the perovskite layer, accelerating its decomposition.[18] To mitigate this, researchers often use an acid passivation strategy, introducing H^+ to neutralize excess OH^- and improve device stability.[19,20] However, external impurities at the buried interface continue to adversely affect charge carrier transport and the photovoltaic performance of PSCs.

The crystallization of the perovskite film in n-i-p structured PSCs is directly influenced by the surface properties of the ETL, significantly affecting the film quality at the buried interface.[21,22] In SnO_2 ETLs, the oxygen vacancies (V_O) or Sn dangling bonds can induce non-radiative recombination, leading to carrier loss at the buried interface and further accelerating device degradation under extreme environmental conditions, such as UV light and heat.[23] Halides, such as chloride derivatives, have been reported to regulate perovskite crystallization and passivate surface defects in SnO_2.[24–26] As a result, various chloride derivatives have been introduced into SnO_2 precursors to modify the interface between perovskite and the ETL by forming chlorine-capped SnO_2 (Cl-SnO_2).[27–30] Cl-SnO_2 has been shown to enhance electron extraction,[31] mitigate interfacial charge recombination,[28]

X. Zhao, D. Wu, H. Yan, P. Cui, Y. Qiu, B. Fan, X. Yue, L. Li, M. Li
State Key Laboratory of Alternate Electrical Power System with Renewable Energy Sources
School of New Energy
North China Electric Power University
Beijing 102206, China
E-mail: mcli@ncepu.edu.cn

The ORCID identification number(s) for the author(s) of this article can be found under https://doi.org/10.1002/smll.202408606

DOI: 10.1002/smll.202408606

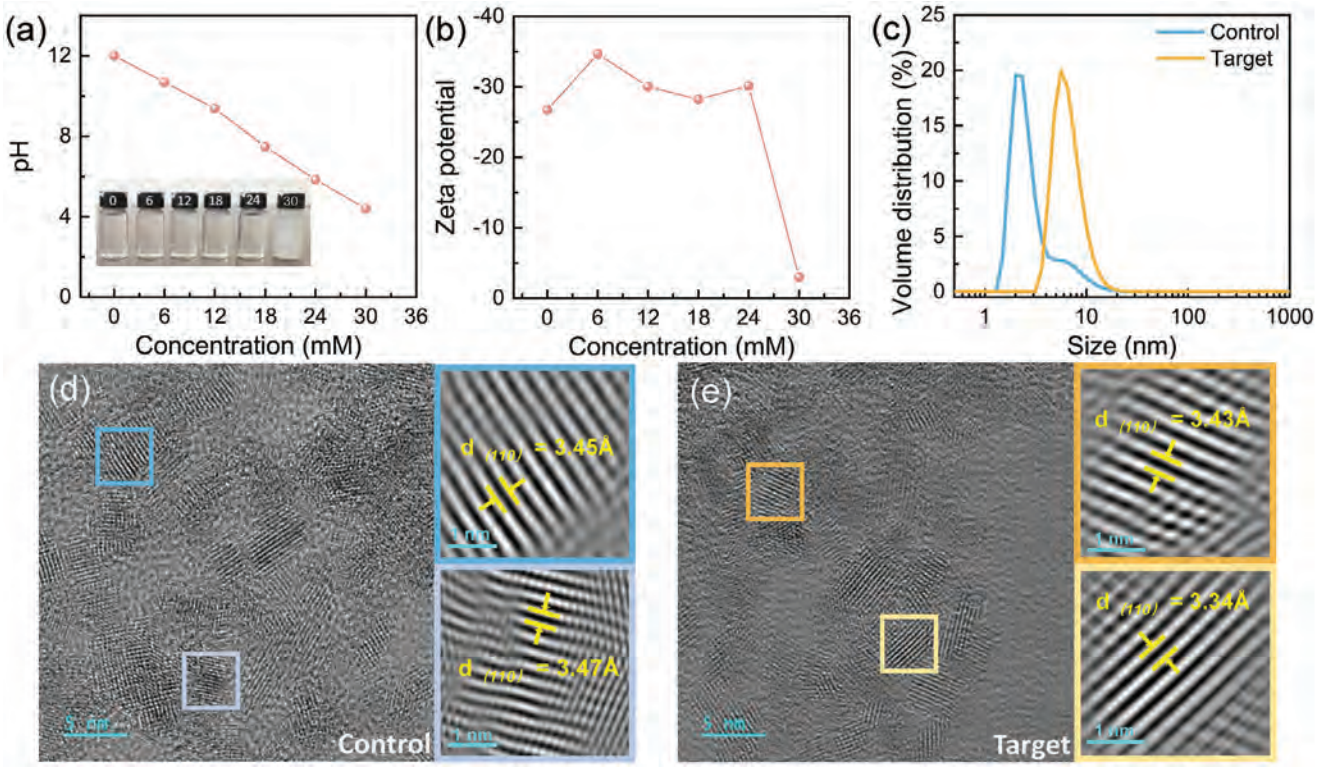

Figure 1. Characterization of SnO_2 precursor solution. a) pH and b) Zeta potential of SnO_2 precursor solutions with different concentrations of HCl. c) Size distribution of control and target SnO_2 solutions. TEM images of d) control and e) target SnO_2 nanoparticles.

and reduce the energy barrier[16] at the ETL/perovskite interface. However, the specific impact of Cl-SnO_2 on the buried interface, the most critical interface in determining the photovoltaic performance of PSCs, has not been thoroughly investigated. To address this, hydrochloric acid (HCl) is considered an ideal candidate for industrial SnO_2. HCl not only counteracts the harmful effects of KOH but also introduces Cl^- ions at the SnO_2/perovskite interface without adding external species. While previous study has explored this interface using HCl,[32] a full understanding of its effects on the buried interface remains incomplete, as the synergistic effects of pH and chlorine doping on the photovoltaic performance and stability of PSCs have yet to be fully explored.

Here, we introduce a small amount of HCl into SnO_2 to mitigate the negative impact of KOH and improve the quality of the buried interface. H^+ ions neutralize OH^- ions, converting KOH into KCl, while Cl^- ions interact with SnO_2, forming Cl-SnO_2. In situ PL analysis shows that the perovskite film deposited on the Cl-SnO_2 ETL undergoes rapid crystallization, enhancing its crystallinity and reducing residual PbI_2 and voids at the buried interface. The champion device using Cl-SnO_2 ETL achieved an impressive certified efficiency of 25.69%. In addition to its high efficiency, the PSC demonstrates excellent air stability, retaining 90% of its initial efficiency after over 2900 h of air exposure. Stability measurements further show that chlorine doping enhances device stability more effectively than pH modification, primarily by promoting perovskite crystallinity and improving the quality of the buried interface.

2. Results and Discussion

In this work, we prepared PSCs with the architecture of ITO/ETL/perovskite/spiro-MeOTAD/Au, using a colloidal SnO_2 solution from Alfa Aesar with KOH as a stabilizer. We measured the pH of SnO_2 precursor solutions with varying HCl concentrations, as shown in **Figure** 1a and Table S1 (Supporting Information). The control SnO_2 solution had a pH of 12.5, confirming its strong basicity. However, as the HCl concentration increased, the pH of the SnO_2 solution gradually decreased. At an HCl concentration of 18 mM, the pH reached neutrality (pH 7.5), indicating an acid-base reaction between KOH and HCl. As the HCl concentration increased to 24 mM, white micelles appeared in the solution, mainly due to the disruption of the alkaline environment. Figure 1b presents the zeta potential measurements. When the HCl concentration was below 24 mM, the zeta potential remained ≈−30 mV. However, at 30 mM, a sharp decrease in zeta potential was observed, suggesting that the colloidal particles had agglomerated. To maintain a neutralized state with fewer OH^- or H^+ ions, we selected the SnO_2 solution with 18 mM HCl as the target sample and the pristine SnO_2 solution as the control sample. Figure 1c shows the dynamic light scattering (DLS) analysis of the SnO_2 nanoparticle size distribution. The average particle size increased from 6.8 nm in the control solution to 12.6 nm in the target solution, likely due to slight aggregation of the SnO_2 nanoparticles. Transmission electron microscopy (TEM) was performed to characterize the morphology of the SnO_2 nanoparticles, as shown in Figure 1d,e, and Figure S1 (Supporting Information). TEM analysis of the SnO_2 crystals reveals a lattice

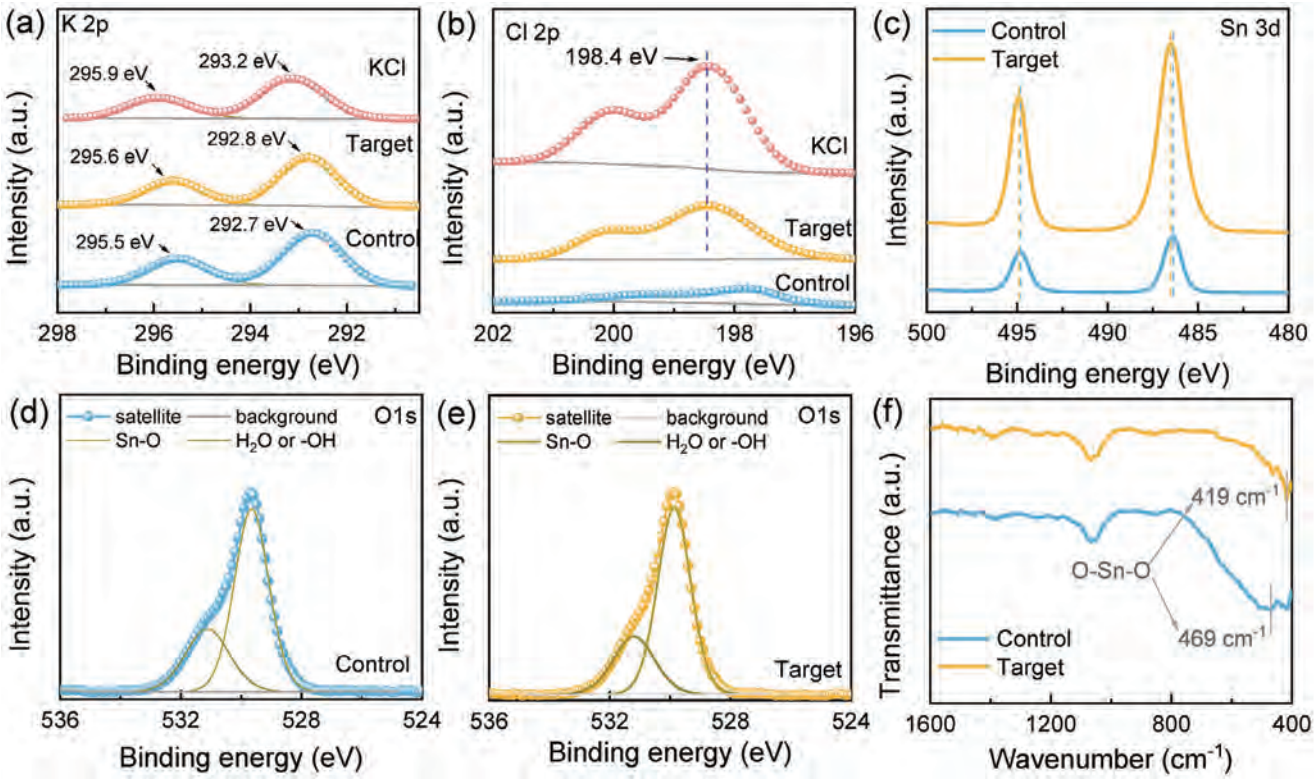

Figure 2. Chemical analysis of SnO_2 ETLs. XPS spectra of a) K 2p, b) Cl 2p, c) Sn 3d, and d,e) O 1s. f) FTIR spectra of control and target SnO_2 films.

spacing of 3.4 Å for both samples, corresponding to the (110) plane of rutile SnO_2. We also assessed the wettability of the control and target ETLs, with the corresponding contact angles shown in Figure S2 (Supporting Information). The contact angle decreased from 14.7° to 13.5°, indicating a slight improvement in wettability, which benefits perovskite deposition. Surface morphologies of the control and target SnO_2 were examined using atomic force microscopy (AFM), as shown in Figure S3 (Supporting Information). The root mean roughness (RMS) slightly increased from 1.85 to 2.63 nm after HCl treatment, ascribing to the increased nanoparticles size.

The chemical composition was analyzed using X-ray photoelectron spectroscopy (XPS) and Fourier-transform infrared (FTIR) spectroscopy, as shown in **Figure 2**. In Figure 2a, the control ETL shows the presence of potassium (K), with the K $2p_{3/2}$ peak at 292.7 eV and the K $2p_{1/2}$ peak at 295.5 eV. However, the K 2p peaks in the target sample shifted to higher binding energies (292.8 and 295.6 eV), indicating the replacement of OH^- with Cl^-adjacent to the K^+ ions. This shift is confirmed by the K 2p peaks of KCl powder, which exhibits the highest binding energy. In Figure 2b, a relatively weak Cl 2p peak from remnants of raw materials is observed in the control sample. In contrast, both the target ETL and KCl films have strong Cl 2p peaks at 198.4 eV, confirming the same chemical state and validating the formation of KCl. In Figure 2c, the Sn 3d spectra of SnO_2 films show slightly higher binding energy in the target sample compared to the control, indicating a chemical interaction between Cl and SnO_2.[33] The O 1s spectra, shown in Figure 2d,e, display a main peak at 530.5 eV corresponding to the Sn═O bond in SnO_2, with a shoulder peak at 531.9 eV indicating the presence of H_2O or hydroxyl groups (−OH) on the SnO_2 surface.[30,34] Quantitative analysis of the peak area ratio ($S_{OH}-/S_{all}$), where S_{OH}^- and S_{all} represent the peak areas of the shoulder and the entire O 1s peak, respectively, reveals the effect of HCl addition to the SnO_2 colloidal solution. The S_{OH}^-/S_{all} ratio decreased from 30.35% for the control ETL to 27.86% for the target ETL, suggesting that the −OH groups on the SnO_2 surface were effectively neutralized by H^+.[35] Additionally, Fourier-transform infrared (FTIR) spectroscopy was utilized to examine the interaction between HCl and SnO_2. Figure 2f shows the O═Sn═O bond stretching peak to lower wavenumbers after HCl treatment, indicating that Cl^- ions altered the electron cloud density around O═Sn═O, consistent with the XPS results.[36]

Since Cl^- ions can promote perovskite crystallization,[37] we investigated the impact of HCl on the buried interface using scanning electron microscopy (SEM) and X-ray diffraction (XRD), as shown in **Figure 3**a–e. The perovskite films were prepared via a sequential deposition method[38] and peeled off following a published protocol.[39] We first characterized the bottom morphologies of the PbI_2 precursor films, as illustrated in Figure 3a–d. The PbI_2 film grown on the target ETL exhibited larger grain size and denser morphology at the bottom compared to the control PbI_2 film, indicating enhanced crystallinity. This was further confirmed by the increased peak intensity in the XRD spectra, shown in Figure 3e. The perovskite films were prepared using the as-deposited PbI_2 precursor films, and their cross-sectional morphologies are shown in Figure 3f,h. The perovskite film on the control ETL shows more grain boundaries than the film on

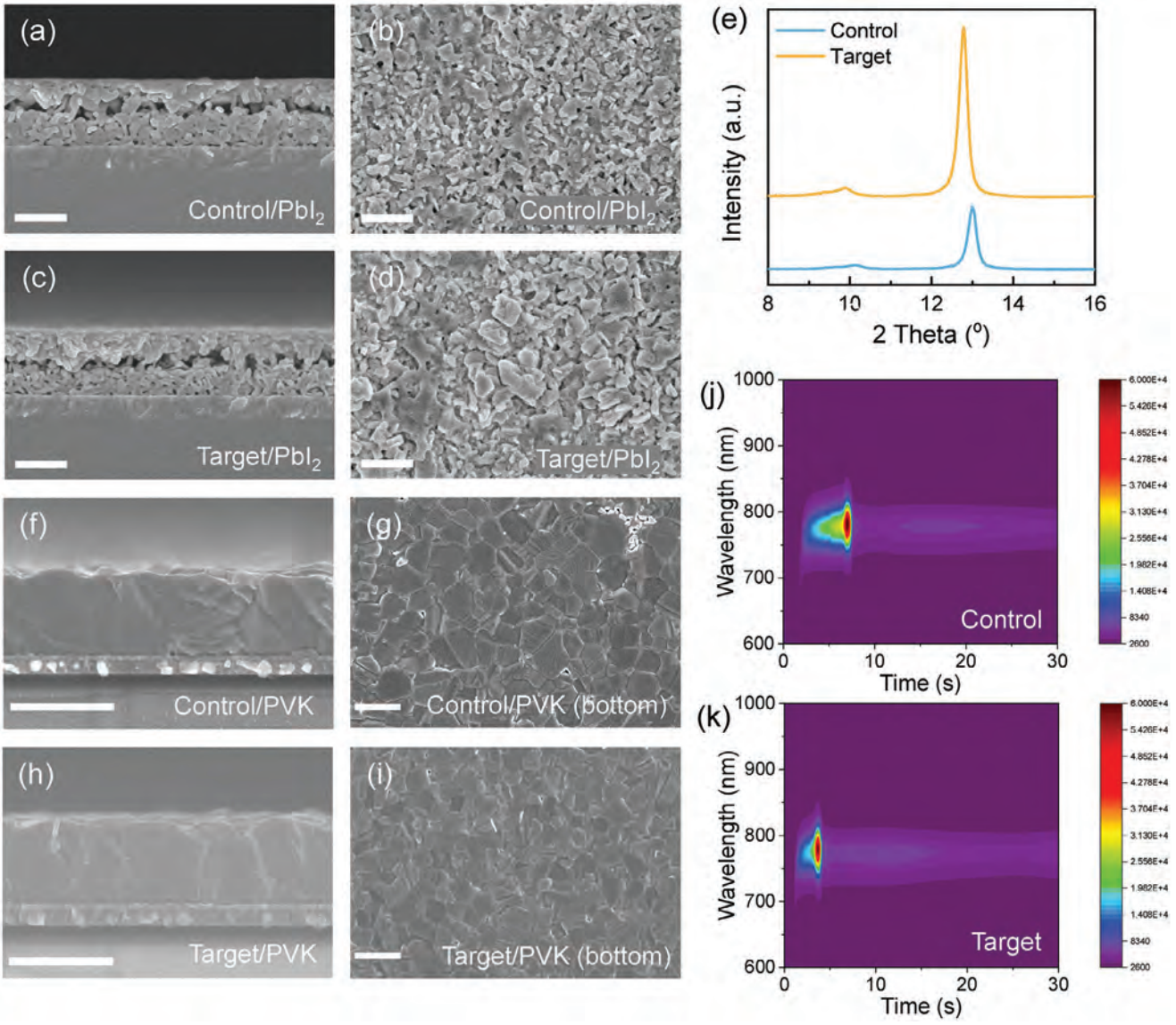

Figure 3. Characterization of PbI_2 and perovskite films. a) Cross-sectional and b) bottom morphology of control PbI_2 film. c) Cross-sectional and d) bottom morphology of target PbI_2 film. e) XRD spectra of PbI_2 films. f) Cross-sectional and g) bottom surface morphology of perovskite film on control ETL. h) Cross-sectional and i) bottom surface morphology of perovskite film on target ETL film. The scale bar is 500 nm. j,k) In situ PL measurement during spin-coating amine salts on PbI_2 substrates.

the target ETL. Finally, we mechanically peeled off the perovskite films and examined their bottom morphologies. In Figure 3g, white clusters and voids are visible in the control perovskite, with the clusters identified as PbI_2 residue at the buried interface.[40] These imperfections contribute to interfacial non-radiative recombination and chemical degradation of the perovskite.[40–42] On the Cl-SnO_2 ETL, the target perovskite film shows a significant improvement in buried interface quality, with no PbI_2 residues or voids. To explore the mechanism behind perovskite crystallization, we performed in situ photoluminescence (PL) measurement during spin-coating of amine salts, as shown in Figure 3j,k. The target perovskite exhibited an earlier peak intensity than the control, indicating a faster crystallization process. This observation aligns with previous reports suggesting that Cl reduces the formation energy of perovskite, thereby promoting its crystallization.[43] The improved crystallinity of the PbI_2 precursor film and the reduced formation energy together enhance the overall film quality of the perovskite films at the bottom surface.

To investigate the change in band structure before and after HCl incorporation, we conducted ultraviolet photoelectron spectroscopy (UPS). The energy level diagrams of the ETL and perovskite films, calculated from the UPS and Tauc plot spectra (Figures S4 and S5, Supporting Information), are shown in **Figure 4a**. After HCl incorporation, the conduction band of the target ETL shifted down to −4.12 eV, and the energy barrier between ETL and perovskite was reduced from 0.31 to 0.19 eV. This reduction enhances charge transport from the perovskite layer to

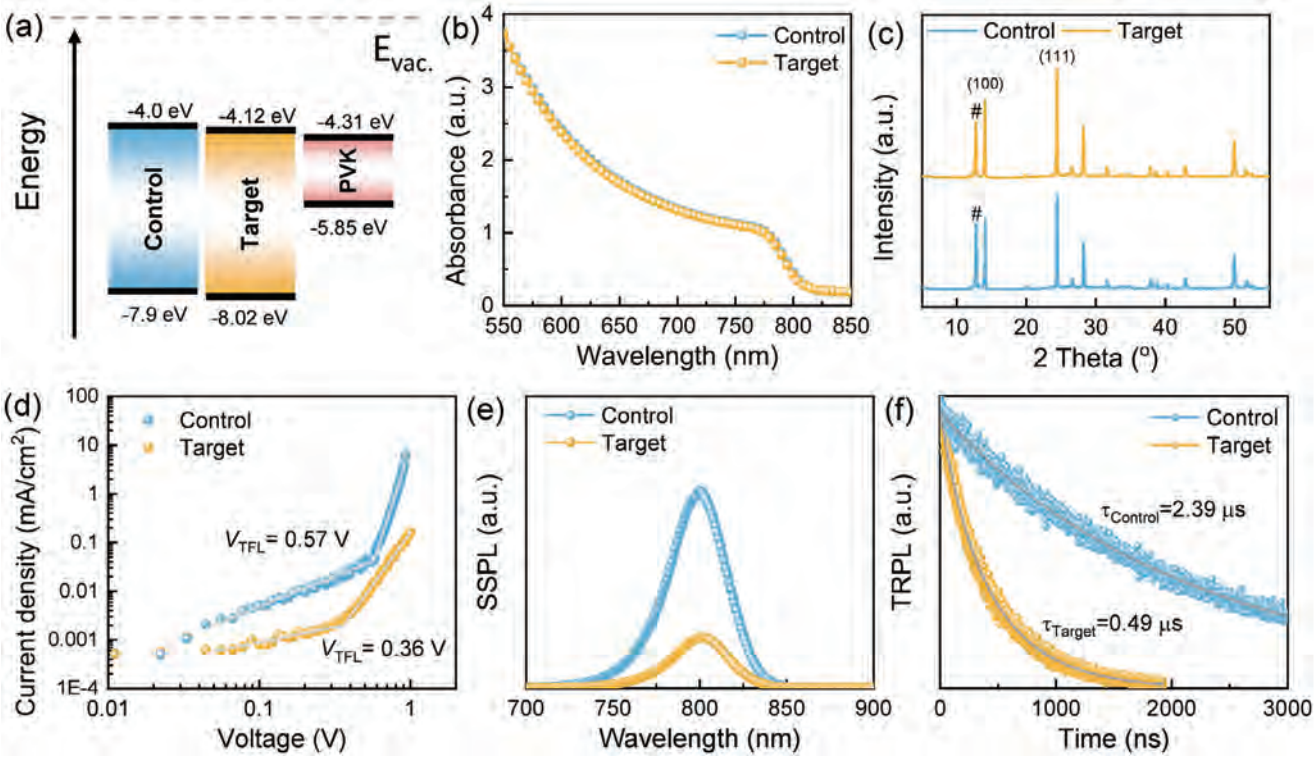

Figure 4. Characterization of perovskite films. a) Energy level diagram of ETLs and perovskite film. b) UV–vis absorbance and c) XRD spectra of perovskite films. d) SCLC curves of the semi-devices based on different ETLs with a configuration of ITO/ETL/perovskite/PCBM/Au. e) SSPL and f) TRPL spectra of perovskite films deposited on different ETL substrates.

the ETL. These findings align with the XPS analysis of Sn 3d, where the shift in binding energy indicates a decrease in the valence state of Sn due to the addition of HCl.[44] The UV–visible spectra of the perovskite films, shown in Figure 4b, reveal similar light absorbance for both samples, suggesting that the addition of HCl does not affect the light absorption properties of the perovskite films. The XRD spectra in Figure 4c show a diffraction peak at 12.8° corresponding to PbI_2 in the perovskite films, while the peaks at 14.1° and 24.4° correspond to the (100) and (111) planes of perovskite, respectively. A decrease in PbI_2 content was observed in the target perovskite, which is attributed to the enhanced crystallinity of the perovskite film induced by Cl^- ions. The trap densities of the perovskite films deposited on different ETLs were characterized using the space charge limited current (SCLC) technique, as shown in Figure 4d. The defect density was calculated according to the formula $N_{trap} = 2\varepsilon\varepsilon_0 V_{TFL}/eL^2$,[45] with the V_{TEL}s determined to be 0.57 and 0.36 V, corresponding to trap densities of 3.25×10^{15} and 2.05×10^{15} cm^{-3} for the control and target perovskite films, respectively. The reduction in trap densities is attributed to the enhanced crystallinity of the perovskite films and the improved quality of the buried interface.[45] To investigate the electron transport and extraction capabilities of the control and target ETLs, as well as charge carrier recombination at the buried interface, steady-state photoluminescence (SSPL) and time-resolved photoluminescence (TRPL) spectroscopy were performed.[44] As shown Figure 4e,f, the target ETL exhibits a stronger quenching effect with a lower PL intensity compared to the control, indicating more efficient charge transfer from the perovskite to the ETL. Additionally, the TRPL curves were fitted using a biexponential decay function to determine the carrier lifetimes, which were calculated to be 2.39 and 0.49 μs for the control and target samples, respectively. The shorter carrier lifetime in the target sample suggests faster charge extraction to the ETL, demonstrating that non-radiative recombination was effectively suppressed.

To further investigate the impact of HCl on the efficiency and stability of PSCs, we fabricated devices using both control and target ETLs. The concentration of HCl added to the ETL precursor was optimized, and the corresponding photovoltaic performance statistics are shown in **Figure** 5a–d. The average PCE increased steadily with HCl concentration, reaching an optimal value at 18 mM from 21.05% to 24.62%, primarily due to improvements in FF (from 76.16% to 83.35%), and V_{OC} (from 1.10 to 1.17 V). However, further increasing the HCl concentration led to a decrease in efficiency, primarily due to the reduction in J_{SC}, caused by the aggregation of SnO_2 nanoparticles. Figure 5e shows that the best-performing PSC, with an 18 mM HCl concentration, achieves an impressive efficiency of 25.39%, with a J_{SC} of 25.63 mA cm^{-2}, a V_{OC} of 1.17 V, and an FF of 84.43%. The certified PCE of the target PSC is 25.69% (Figure S6, Supporting Information), the highest reported for PSCs based on Cl-SnO_2 ETLs (Figure 5f). We also prepared 1 cm^2 PSC, and the *J–V* curves for both reverse and forward scan directions are shown in Figure 5g, with an efficiency of 24% at reverse scan. The

External quantum efficiency (EQE) curves of the control and target PSCs are shown in Figure 5f, with the integrated J_{SC}

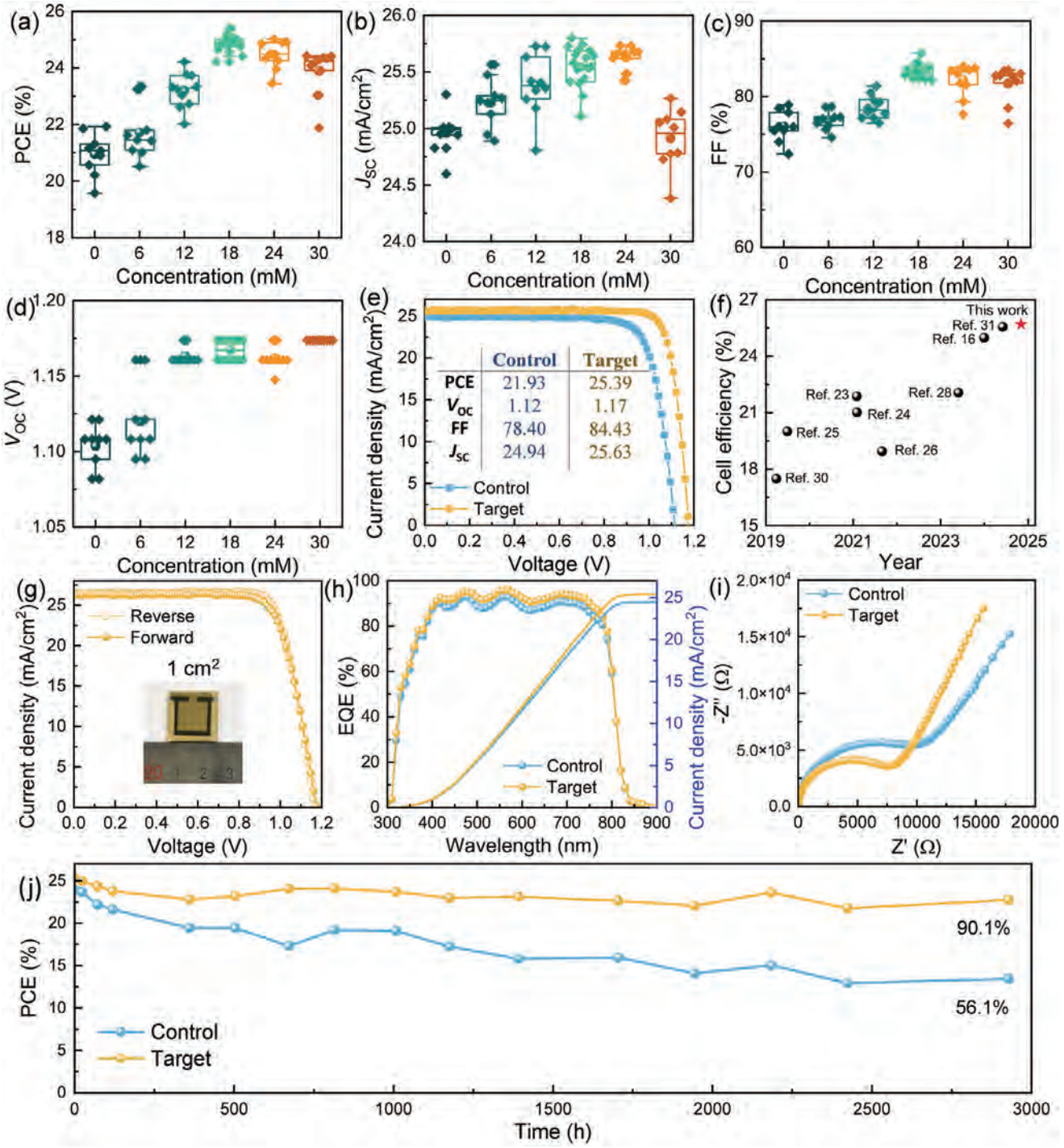

Figure 5. Photovoltaic performance and stability of PSCs. a–d) Statistic photovoltaic performance of the PSCs with different concentrations of HCl. e) Best-performing *J–V* curves of the control and target PSCs with an active area of 0.1 cm^2. f) Efficiency chart of PSCs using Cl-SnO_2 ETL. g) *J–V* curves of 1 cm^2 PSC with reverse and forward scan direction. h) EQE spectra of the control and target PSCs. i) EIS spectra of the control and target PSCs. j) Air-stability of the PSCs stored in a drying closet with a humidity of ± 10%.

improved from 24.89 to 25.23 mA cm^{-2}, closely matching the J_{SC} values obtained from the *J–V* curves. Electrochemical impedance spectroscopy (EIS) was performed to characterize interfacial charge transfer and recombination in PSCs. Figure 5i displays the Nyquist plots of the PSCs with control and target ETLs measured under dark condition. The series resistance (R_s) of the target PSC is lower at 11.77 Ω compared to 16.68 Ω for the control PSC. The charge transfer resistance (R_{tr}) decreases from 3.4 × 10^4 Ω for the control PSC to 8.3 × 10^3 Ω for the target PSC, indicating more efficient charge transfer in the target PSC.

Additionally, the charge recombination resistance (R_{rec}) increases from 1.05×10^4 Ω for the control PSC to 3.52×10^4 Ω for the target PSC, reflecting reduced non-radiative recombination at the buried interface.

The properties of ETL layers are critical to the quality of the buried interface and directly influence device stability. Incorporating HCl not only adjusts the pH of the SnO_2 precursor solution but also increases its chlorine content. To further investigate the effects of pH and chlorine content on device stability, we fabricated PSCs treated with varying HCl concentrations. The unencapsulated PSCs were stored in a drying closet at a relative humidity (RH) of 15%±5% and measured under ambient air at 45±5% RH. The stability of PSCs treated with different HCl concentrations is summarized in Figure S7 (Supporting Information). Control devices with a high pH of 12.5 showed a sharp efficiency drop after 72 h, while PSCs treated with varying HCl concentrations (pH 10.7 to 4.4) exhibited no significant difference in efficiency, indicating that pH alone does not play a decisive role in PSC stability. For the device treated with 18 mM HCl (pH 7.5), Figure 5j shows that it retains 90% of its initial efficiency after over 2900 h, whereas the control PSC retains only 56.1%, demonstrating excellent air stability in the HCl treated PSC. Figure S8 (Supporting Information) shows the steady-state current output of the target PSC measured under 1-sun illumination in air at 30% RH. After 300 s, the current density remained nearly constant, further confirming its excellent operational stability.

In addition, KOH additives or by-product KCl inevitably remain in the ETL films, impacting the photovoltaic performance and stability of PSCs. To further investigate the roles of pH and chlorine doping, we washed the pristine SnO_2 films in DI-H_2O to remove ionic residues, then spin-coated them with 18 mM solutions of HCl, KCl, and KOH, with pH values of 2.4, 6.8, and 12.17, respectively. This washing process ensures the removal of KOH from pristine SnO_2 and does not alter surface morphologies, as shown in Figure S9 (Supporting Information). Statistical photovoltaic performance of PSCs based on different SnO_2 ETLs, with and without DI-H_2O washing, is shown in Figure S10 (Supporting Information), while maximum power point tracking (MPPT) results for each device in air are shown in Figure S11 (Supporting Information). Interestingly, chlorine-containing devices (including target Cl-SnO_2, washed SnO_2 + HCl, and washed SnO_2 + KCl ETLs) maintained better stability, while devices without chlorine (control SnO_2 and washed SnO_2 + KOH ETLs) experienced a significant decline. These results suggest that chlorine doping enhances device stability more effectively than pH modification, primarily due to the role of chlorine in promoting perovskite crystallinity and improving the quality of the buried interface in PSCs.

3. Conclusion

In this work, we propose a straightforward approach to synergistically optimize the buried interface in PSCs by incorporating HCl into commercial SnO_2. Multiple positive effects are superimposed using this strategy, including converting detrimental KOH into KCl, reducing PbI_2 residues and voids, and improving band alignment at the buried interface. Finally, we achieved a certified efficiency of 25.69% for the target PSC, the highest efficiency achieved for PSCs based on Cl-SnO_2 ETLs. Moreover, the modified target PSC demonstrates excellent air stability, retaining 90% of its initial efficiency after over 2900 h in dry air, compared to only 56% for the control PSC. The role of chlorine doping in enhancing device stability has also been confirmed, primarily through its ability to promote perovskite crystallinity and improve the quality of the buried interface. Finally, the improved quality of the buried interface, coupled with enhanced efficiency and stability, makes this strategy highly promising for future applications in PSCs.

Supporting Information

Supporting Information is available from the Wiley Online Library or from the author.

Acknowledgements

X.Z. and D.W. contributed equally to this work. This work was supported partially by the Key Research and Development Program sponsored by the Ministry of Science and Technology (MOST) (Grant no. 2022YFB4200301), National Natural Science Foundation of China (Grant nos. 22409061, 52232008, 51972110, 52102245, 52072121, and 52402254), the Beijing Natural Science Foundation (2222076 and 2222077), the Beijing Nova Program (20220484016), Young Elite Scientists Sponsorship Program by CAST (2022QNRC001), 2022 Strategic Research Key Project of Science and Technology Commission of the Ministry of Education, the Huaneng Group Headquarters Science and Technology Project (HNKJ20-H88), the State Key Laboratory of Alternate Electrical Power System with Renewable Energy Sources (LAPS2024-05), the Fundamental Research Funds for the Central Universities (2022MS029, 2022MS02, 2022MS031, 2023MS042, and 2023MS047) and the NCEPU "Double First-Class" Program.

Conflict of Interest

The authors declare no conflict of interest.

Data Availability Statement

The data that support the findings of this study are available from the corresponding author upon reasonable request.

Keywords

buried interface, Cl-SnO_2, hydrochloric acid, KOH, perovskite solar cells

Received: September 20, 2024
Revised: November 21, 2024
Published online: December 26, 2024

[1] H.-S. Kim, C.-R. Lee, J.-H. Im, K.-B. Lee, T. Moehl, A. Marchioro, S.-J. Moon, R. Humphry-Baker, J.-H. Yum, J. E. Moser, M. Grätzel, N.-G. Park, *Sci. Rep.* **2012**, *2*, 591.
[2] T. Miyasaka, *Chem. Lett.* **2015**, *44*, 720.
[3] M. Saliba, *Science* **2018**, *359*, 388.
[4] A. Kojima, K. Teshima, Y. Shirai, T. Miyasaka, *J. Am. Chem. Soc.* **2009**, *131*, 6050.
[5] National Renewable Energy Laboratory, Best Research-Cell Efficiency Chart (accessed: November 2024), https://www.nrel.gov/pv/cell-efficiency.html/.

[6] X. Yang, D. Luo, Y. Xiang, L. Zhao, M. Anaya, Y. Shen, J. Wu, W. Yang, Y. H. Chiang, Y. Tu, R. Su, Q. Hu, H. Yu, G. Shao, W. Huang, T. P. Russell, Q. Gong, S. D. Stranks, W. Zhang, R. Zhu, *Adv. Mater.* **2021**, *33*, 2006435.
[7] B. Chen, P. N. Rudd, S. Yang, Y. Yuan, J. Huang, *Chem. Soc. Rev.* **2019**, *48*, 3842.
[8] X. Ji, L. Bi, Q. Fu, B. Li, J. Wang, S. Y. Jeong, K. Feng, S. Ma, Q. Liao, F. R. Lin, H. Y. Woo, L. Lu, A. K. Y. Jen, X. Guo, *Adv. Mater.* **2023**, *35*, 2303665.
[9] J. Du, J. Yuan, H. Wang, F. Huang, J. Tian, *ACS Appl. Energy Mater.* **2022**, *5*, 1914.
[10] C. Ge, L. Xie, J. Yang, K. Wei, T. Wu, L. Wang, L. Sun, J. Zhang, Y. Hua, *Adv. Funct. Mater.* **2024**, *34*, 2313688.
[11] X. Wang, H. Huang, M. Wang, Z. Lan, P. Cui, S. Du, Y. Yang, L. Yan, Q. Zhang, S. Qu, M. Li, *Adv. Mater.* **2024**, *36*, 2310710.
[12] Q. Jiang, L. Zhang, H. Wang, X. Yang, J. Meng, H. Liu, Z. Yin, J. Wu, X. Zhang, J. You, *Nat. Energy* **2016**, *2*, 16177.
[13] T. Bu, J. Li, F. Zheng, W. Chen, X. Wen, Z. Ku, Y. Peng, J. Zhong, Y.-B. Cheng, F. Huang, *Nat. Commun.* **2018**, *9*, 4609.
[14] D. Garcia Romero, L. Di Mario, F. Yan, C. M. Ibarra-Barreno, S. Mutalik, L. Protesescu, P. Rudolf, M. A. Loi, *Adv. Funct. Mater.* **2024**, *34*, 2307958.
[15] S. You, H. Zeng, Z. Ku, X. Wang, Z. Wang, Y. Rong, Y. Zhao, X. Zheng, L. Luo, L. Li, S. Zhang, M. Li, X. Gao, X. Li, *Adv. Mater.* **2020**, *32*, 2003990.
[16] Y. Wang, M. Feng, H. Chen, M. Ren, H. Wang, Y. Miao, Y. Chen, Y. Zhao, *Adv. Mater.* **2024**, *36*, 2305849.
[17] Y. Hu, Z. He, X. Jia, W. Zhao, S. Zhang, M. M. Jiao, Q. Xu, D. Wang, C. Yang, G. Yuan, L. Han, *Sol. RRL* **2022**, *6*, 2100942.
[18] Z. Liu, L. Qiu, L. K. Ono, S. He, Z. Hu, M. Jiang, G. Tong, Z. Wu, Y. Jiang, D.-Y. Son, Y. Dang, S. Kazaoui, Y. Qi, *Nat. Energy* **2020**, *5*, 596.
[19] Q. Geng, X. Jia, Z. He, Y. Hu, Y. Gao, S. Yang, C. Yao, S. Zhang, *Adv. Mater. Interfaces.* **2022**, *9*, 2201641.
[20] H. S. Yun, Y. H. Seo, C. E. Seo, H. S. Kim, S. Bin Yoo, B. J. Kang, N. J. Jeon, E. H. Jung, *Adv. Energy Mater.* **2024**, *14*, 2400791.
[21] S. Zhang, F. Ye, X. Wang, R. Chen, H. Zhang, L. Zhan, X. Jiang, Y. Li, X. Ji, S. Liu, M. Yu, F. Yu, Y. Zhang, R. Wu, Z. Liu, Z. Ning, D. Neher, L. Han, Y. Lin, H. Tian, W. Chen, M. Stolterfoht, L. Zhang, W. H. Zhu, Y. Wu, *Science* **2023**, *380*, 404.
[22] M. Wang, A. He, L. Wu, X. Hao, G. Xia, Y. Jiang, R. Su, J. Zhang, *J. Mater. Chem. A* **2023**, *11*, 19496.
[23] L. Zhang, H. Ma, Z. Ying, Q. Dong, M. Yuan, S. Rong, Z. Wang, S. Wang, S. Li, J. Zhang, D. Cao, W. Han, Y. Yan, W. Tian, J. Bian, Y. Shi, *Adv. Funct. Mater.* **2024**, *34*, 2406946.
[24] Z. Lin, W. Zhang, Q. Cai, X. Xu, H. Dong, C. Mu, J. P. Zhang, *Adv. Sci.* **2021**, *8*, 2102845.
[25] P. Song, L. Shen, L. Zheng, K. Liu, W. Tian, J. Chen, Y. Luo, C. Tian, L. Xie, Z. Wei, *Nano. Sel.* **2021**, *2*, 1779.
[26] P. Chen, W. Pan, S. Zhu, F. Cao, A. Tong, R. He, Z. Lan, W. Sun, J. Wu, *Chem. Eng. J.* **2023**, *468*, 143652.
[27] J. B. Wu, C. Zhen, G. Liu, *Rare Met.* **2022**, *41*, 361.
[28] J. Liang, Z. Chen, G. Yang, H. Wang, F. Ye, C. Tao, G. Fang, *ACS Appl. Mater. Interfaces.* **2019**, *11*, 23152.
[29] P. Zhu, S. Gu, X. Luo, Y. Gao, S. Li, J. Zhu, H. Tan, *Adv. Energy Mater.* **2020**, *10*, 1903083.
[30] Z. Xiong, X. Chen, B. Zhang, G. O. Odunmbaku, Z. Ou, B. Guo, K. Yang, Z. Kan, S. Lu, S. Chen, N. A. N. Ouedraogo, Y. Cho, C. Yang, J. Chen, K. Sun, *Adv. Mater.* **2022**, *34*, 2106118.
[31] J. W. Song, Y. S. Shin, M. Kim, J. Lee, D. Lee, J. Seo, Y. J. Lee, W. Lee, H. B. Kim, S. I. Mo, J. H. An, J. E. Hong, J. Y. Kim, I. Jeon, Y. Jo, D. S. Kim, *Adv. Energy Mater.* **2024**, *14*, 2401753.
[32] Y. Li, J. Meng, P. Duan, R. Wu, Y. Shi, L. Zhang, C. Yan, J. Deng, X. Zhang, *ACS Appl. Mater. Interfaces.* **2023**, *15*, 23208.
[33] H. Virieux, M. Le Troedec, A. Cros-Gagneux, W. S. Ojo, F. Delpech, C. Nayral, H. Martinez, B. Chaudret, *J. Am. Chem. Soc.* **2012**, *134*, 19701.
[34] J. Fan, Y. Dai, Y. Li, N. Zheng, J. Guo, X. Yan, G. D. Stucky, *J. Am. Chem. Soc.* **2009**, *131*, 15568.
[35] C. Liu, J. Zhang, L. Zhang, X. Zhou, Y. Liu, X. Wang, B. Xu, *Adv. Energy Mater.* **2022**, *12*, 2200945.
[36] J. Deng, K. Wei, L. Yang, L. Lin, Y. Xiao, X. Cai, C. Zhang, D. Wu, X. Zhang, J. Zhang, *Adv. Mater.* **2023**, *35*, 2300233.
[37] M. Kim, G. H. Kim, T. K. Lee, I. W. Choi, H. W. Choi, Y. Jo, Y. J. Yoon, J. W. Kim, J. Lee, D. Huh, H. Lee, S. K. Kwak, J. Y. Kim, D. S. Kim, *Joule* **2019**, *3*, 2179.
[38] X. Zhao, Y. Qiu, M. Wang, D. Wu, X. Yue, H. Yan, B. Fan, S. Du, Y. Yang, Y. Yang, D. Li, P. Cui, H. Huang, Y. Li, N. G. Park, M. Li, *ACS Energy Lett.* **2024**, *9*, 2659.
[39] Z. Dai, S. K. Yadavalli, M. Chen, A. Abbaspourtamijani, Y. Qi, N. P. Padture, *Science* **2021**, *372*, 618.
[40] Y. Gao, F. Ren, D. Sun, S. Li, G. Zheng, J. Wang, H. Raza, R. Chen, H. Wang, S. Liu, P. Yu, X. Meng, J. He, J. Zhou, X. Hu, Z. Zhang, L. Qiu, W. Chen, Z. Liu, *Energy Environ. Sci.* **2023**, *16*, 2295.
[41] W. Shao, H. Wang, F. Ye, C. Wang, C. Wang, H. Cui, K. Dong, Y. Ge, T. Wang, W. Ke, G. Fang, *Energy Environ. Sci.* **2022**, *16*, 252.
[42] M. Wang, C. Fei, M. A. Uddin, J. Huang, *Sci. Adv.* **2022**, *8*, eabo5977.
[43] X. Liu, Y. Guo, Y. Cheng, S. Lu, R. Li, J. Chen, *Chem. Commun.* **2023**, *59*, 13394.
[44] S. Y. Kim, F. Zhang, J. Tong, X. Chen, E. Enkhbayar, K. Zhu, J. H. Kim, *Sol. Energy* **2022**, *233*, 353.
[45] L. Yang, H. Zhou, Y. Duan, M. Wu, K. He, Y. Li, D. Xu, H. Zou, S. Yang, Z. Fang, S. Liu, Z. Liu, *Adv. Mater.* **2023**, *35*, 2211545.

